JGR Space Physics

RESEARCH ARTICLE
10.1029/2024JA032697

Key Points:

- Local models of peak electron density for 43 low-mid latitude ionosondes are developed. Models capture known global ionospheric features
- Approximately 8 years of minimum data coverage is required to describe the solar activity dependence of peak electron density
- Models driven by the Flare Irradiance Spectral Model are more accurate than models driven by F10.7 and the IRI-2020 model

Supporting Information:

Supporting Information may be found in the online version of this article.

Correspondence to:

D. Singh and L. P. Goncharenko,
dupinder@mit.edu;
lpg@mit.edu

Citation:

Singh, D., Goncharenko, L. P., Galkin, I. A., Chamberlin, P. C., & Redondo, F. (2024). Local empirical modeling of NmF2 using ionosonde observations and the FISM2 solar EUV model. *Journal of Geophysical Research: Space Physics*, *129*, e2024JA032697. https://doi.org/10.1029/2024JA032697

Received 29 MAR 2024
Accepted 26 AUG 2024

Local Empirical Modeling of NmF2 Using Ionosonde Observations and the FISM2 Solar EUV Model

D. Singh[1], L. P. Goncharenko[1,2], I. A. Galkin[3], P. C. Chamberlin[4], and F. Redondo[5]

[1]Haystack Observatory, Massachusetts Institute of Technology, Westford, MA, USA, [2]Leibniz Institute of Atmospheric Physics at the University of Rostock, Kühlungsborn, Germany, [3]University of Massachusetts Lowell, Lowell, MA, USA, [4]Laboratory for Atmospheric Physics, University of Colorado, Boulder, CO, USA, [5]Clemson University, Clemson, SC, USA

Abstract Local empirical models of the F2 layer peak electron density (NmF2) are developed for 43 low-middle latitude ionosonde stations using auto-scaled data from Lowell GIRO data center and manually scaled data from World Data Center for Ionosphere and Space Weather. Data coverage at these stations ranges from a few years to up to 6 decades. Flare Irradiance Spectral Model index version 2 (FISM2) and ap3 index are used to parametrize the solar extreme ultraviolet (EUV) flux and geomagnetic activity dependence of NmF2. Learning curves suggest that approximately 8 years of data coverage is required to constrain the solar activity dependence of NmF2. Output of local models altogether captures well known anomalies of the F2 ionospheric layer. Performance metrics demonstrate that the model parametrized using FISM2 has better accuracy than a similarly parametrized model with F10.7, as well as than the IRI-2020 model. Skill score metrics indicate that the FISM2 based model outperforms F10.7 model at all solar activity levels. The improved accuracy of model with FISM2 over F10.7 is due to better representation of solar rotation by FISM2, and due to its performance at solar extremum. Application of singular spectrum analysis to model output reveals that solar rotation contributes to about 2%–3% of the variance in NmF2 data and FISM2 based model, while F10.7 based models overestimate the strength of solar rotation to be at 4%–7%. At solar extremum, both F10.7-based model and IRI-2020 tend to overestimate the NmF2 while FISM2 provides the most accurate prediction out of three.

Plain Language Summary We developed local empirical models of peak electron density (NmF2) that describe its variation with solar activity, geomagnetic activity, and season. The NmF2 data for this model comes from 43 ionosonde stations all over the world. Our local models capture well known global characteristics of the NmF2. Further, we show that the solar activity dependence of NmF2 is better explained using the FISM2 which is an empirical model of solar EUV variability. Data-model comparison reveals that FISM2 based model of NmF2 is more accurate than a F10.7 based model and significantly more accurate than the IRI-2020 model. Among the three models, FISM2 provides the most accurate representation of the solar rotation signal in NmF2 and a better prediction of NmF2 during periods of solar maximum and minimum.

1. Introduction

Ionospheric F2 layer peak electron density (NmF2) is an important ionospheric parameter due to its application to HF radio communication, satellite-based navigation, radio astronomy, and space weather prediction (e.g., Cander, 2019 and references therein; De Gasperin et al., 2018). Several physical and empirical models of different ionospheric quantities including NmF2 have been developed in the past and used for both operational and research purposes. Because of the computational cost associated with physical models and gaps in the understanding of ionosphere system, empirical models continue to play an important role for both applications and academic research. Ionospheric empirical models are also used for data reduction purposes wherein the variability from known drivers is removed from the ionospheric data sets. A typical application of ionosphere data reduction is for resolving long-term trends (e.g., Zossi et al., 2023) and interannual variability of ionospheric parameters. International Reference Ionosphere (IRI) and NeQuick are the two most widely used empirical models of the ionosphere (Bilitza et al., 2022; Nava et al., 2008).

Unlike their physical counterpart, whose prediction capability is limited by the state of knowledge of the physical system, the accuracy of empirical models is as good as the available historical observations and proxies for the explanatory variables. Therefore, continuous, and consistent observation of ionospheric parameters and the drivers of their variability is critical to constraining the dependency of the ionosphere on its drivers. The strongest driver for the variability of the ionosphere is solar Extreme Ultraviolet (EUV) radiation. EUV cannot be monitored from the ground due to its strong absorption by the atmosphere, while satellite-based observations of EUV are challenging and include long data gaps (Cessateur et al., 2012; Donnelly, 1987; Woods et al., 2005). Space based EUV instruments are subjected to the harsh space environment and require periodic calibration to address the degradation of various components (e.g., BenMoussa et al., 2013; Woods et al., 2018).

Due to the limited availability of direct EUV observations of the Sun, researchers have employed various proxies to estimate solar EUV-related variability and its impact on the Earth's ionosphere. Of these, the F10.7 index is the most widely used proxy among the ionosphere community. F10.7 is the 10.7 cm microwave flux emitted by solar chromosphere and corona, and it is strongly correlated with solar EUV flux. Unlike EUV, the 10.7 cm flux faces little attenuation by the atmosphere and requires inexpensive monitoring hardware that faces little degradation over long time and is easy to calibrate. Tapping and Morgan (2017) noted a 2% calibration change when radio telescopes were relocated from Ottawa to Penticton. While F10.7 helps to explain the monthly mean state of ionosphere, it does not fully capture the short-term variability of ionosphere driven by solar EUV. To remedy the drawbacks of these proxies, several solar EUV spectral models have been developed by parametrizing available EUV observations with proxies (e.g., Chamberlin et al., 2007, 2020; Hinteregger et al., 1981; Lean et al., 2003; Richards et al., 2006; Thiemann et al., 2019; Tobiska, 2004; Warren et al., 2001).

There are several discrepancies in using F10.7 as a proxy for solar EUV variability. First is the strong short-term variability in F10.7 that is not seen in EUV (de Wit et al., 2008; Donnelly et al., 1983; Hinteregger, 1981; Schonfeld et al., 2019). Some of the short-term variability in the F10.7 index can be attributed to the fact that F10.7 daily averages are undersampled, making them sensitive to transient solar events (Tapping & Charrois, 1994). Second is non-linearity between F10.7 and EUV observations (e.g., Balan et al., 1994; Liu et al., 2006; Richards et al., 1994). Third is its bottoming-out at low solar activity (Chamberlin et al., 2007; Chen et al., 2011). Some studies have used a modified F10.7 index $\text{F10.7P} = (\text{F10.7} + \text{F10.7}_{81})/2$ to remove some of the non-linearity and short-term variability from the F10.7 index (e.g., Hinteregger et al., 1981; Liu et al., 2006; Richards et al., 1994). Because EUV and F10.7 emissions originate from different region of sun through distinctive physical mechanisms, they are expected to have different variability driven by subtle difference between the solar rotation modulation of these emissions pertaining to different optical thickness of their source regions.

This paper describes the development of local empirical models of NmF2 based on data from 43 ionosonde stations and the FISM2 model of solar EUV. Combined output of the local models is tested to examine how well it captures the known global ionospheric features. The predictive performance of FISM2-based model is compared against a similarly parametrized model with the F10.7 index, and the IRI-2020 model (Bilitza et al., 2022). Different metrics discriminated against the solar activity are used to assess the performance of these models at different solar activity levels with special attention paid to the periods of solar minima and maxima. We also explore the suitability of F10.7 and FISM2 to reproduce the solar rotation modulation of NmF2.

2. Data and Methodology

2.1. Ionosonde Data

This study utilizes ionosonde data obtained from 43 low to mid-latitude ionosonde stations, spanning from few years to several decades of data coverage. Of these, 37 stations are available from the Lowell GIRO (Global Ionospheric Radio Observatory) Data Center (LGDC) (Reinisch & Galkin, 2011), while the remaining 6 stations are sourced from the World Data Center (WDC) for Ionosphere and Space Weather, operated by the National Institute of Information and Communication Technology (NICT). Note that the LGDC data is auto scaled, while WDC data is manually scaled. The geographical locations of the ionosonde stations and their data coverage are depicted in the top and bottom panels, respectively, of Figure 1. Table 1 lists the names, short names, geographical coordinates, magnetic latitude, and the scaling method of the stations used in current study. The parameter used in current study is F2 region peak electron density (NmF2). Data is preprocessed to eliminate outliers, then gridded to 30 min resolution and subjected to a low-pass filter to remove variations with time periods less than 6 hr. Outliers are filtered out using a Hampel filter with a window size of 3 and a standard deviation threshold of 3 (Liu et al., 2004). Leap days are excluded from the modeling data set to simplify representation of seasonal cycle for different years.

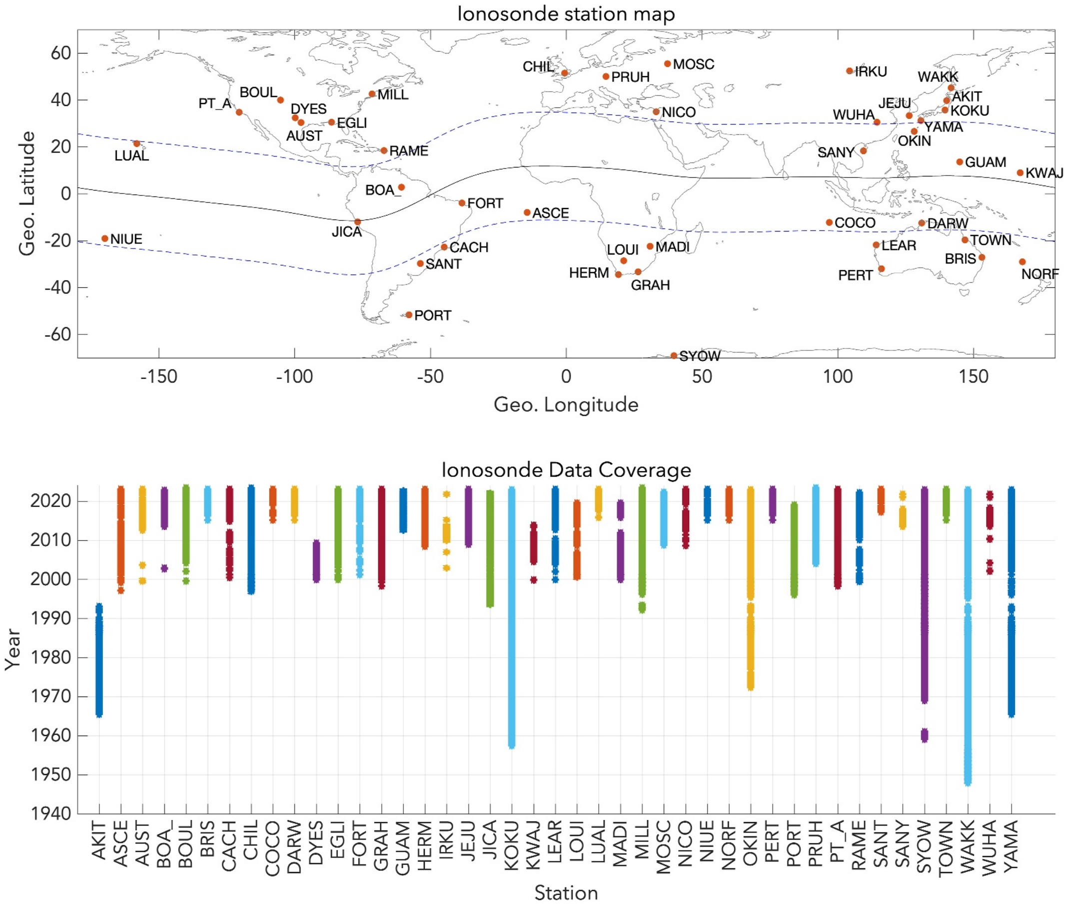

Figure 1. Geographical location of ionosonde stations used in current study (top) and their temporal data coverage (bottom). Black line marks the Quasi-dipole equator as of 2020. Dashed blue lines mark the location of EIA crest (±23 QD latitude).

At some stations, there were instances when autoscaled data shows saturation around noontime, particularly during high solar activity. This issue was attributed to problems with auto-scaling. The impact of such data on model prediction is discussed in Text S2 of the Supporting Information S1, focusing on the GRAH station. Note that the Confidence Score, as noted in previous studies (e.g., Chartier et al., 2023), does not effectively identify problems in the autoscaled data.

2.2. Solar EUV Proxies

We utilize daily values of Flare Irradiance Spectral Model-Version 2 (FISM2) as EUV proxy to model the solar irradiance dependence of NmF2. FISM2 is a spectrally resolved empirical model of solar EUV variability in the wavelength range of 0.01–190 nm. It incorporates observations from multiple spacecraft instruments including SDO EVE (Woods et al., 2012), SORCE SOLSTICE (McClintock et al., 2005), and SORCE XPS (Woods et al., 2005) to model daily EUV irradiance (Chamberlin et al., 2007, 2020). During the time periods when EUV observations are not available, FISM2 uses different proxies as a backup for different EUV bands including the F10.7 index, MgII c/w (Snow et al., 2005), and the H1 Lyman-α (Woods et al., 2000). The selection of proxy for each wavelength is based on their formation temperature and location in solar atmosphere (Chamberlin et al., 2007). FISM2 daily model is obtained by separately modeling the three components at each wavelength that is, the solar minimum reference, the solar cycle component, and the solar rotation component. The estimation of the first two components involves using a 108-day smoothed time series of measurements and proxies, with only the available days included in the smoothing process for near real-time estimations. Reader is referred to Chamberlin et al. (2020) for the detailed parametrization scheme of FISM2.

Table 1
List of Ionosonde Stations Used in Current Study

Station	Short name	Latitude	Longitude	QD lat. (2020)	Scaling
Akita	AKIT	39.7	140.1	33	Manual
Ascension Island	ASCE	−8	−14.4	−19.6	Auto
Austin	AUST	30.4	−97.7	39.6	Auto
Boa Vista	BOA_	2.8	−60.7	8.9	Auto
Boulder	BOUL	40	−105.3	48.1	Auto
Brisbane	BRIS	−27.1	153.1	−35.7	Auto
Cachoeira Paulista	CACH	−22.7	−45	−20.6	Auto
Chilton	CHIL	51.5	−0.6	47.5	Auto
Cocos Island	COCO	−12.2	96.8	−21.5	Auto
Darwin	DARW	−12.5	131	−21.2	Auto
Dyess Afb	DYES	32.4	−99.8	41.3	Auto
Eglin Afb	EGLI	30.5	−86.5	40.4	Auto
Fortaleza	FORT	−3.9	−38.4	−8.7	Auto
Grahamstown	GRAH	−33.3	26.5	−41.5	Auto
Guam	GUAM	13.6	144.9	6	Auto
Hermanus	HERM	−34.4	19.2	−42.3	Auto
Irkutsk	IRKU	52.4	104.3	48.1	Auto
Jeju	JEJU	33.4	126.3	27.3	Auto
Jicamarca	JICA	−12	−76.8	−0.5	Auto
Kokubunji	KOKU	35.7	139.5	28.9	Manual
Kwajalein	KWAJ	9	167.2	3.7	Auto
Learmonth	LEAR	−21.8	114.1	−31.7	Auto
Louisvale	LOUI	−28.5	21.2	−38	Auto
Lualualei	LUAL	21.4	−158.1	21.1	Auto
Madimbo	MADI	−22.4	30.9	−32.3	Auto
Millstone Hill	MILL	42.6	−71.5	50.6	Auto
Moscow	MOSC	55.5	37.3	51.8	Auto
Nicosia	NICO	35	33.2	29.6	Auto
Niue	NIUE	−19.1	−169.9	−21.1	Auto
Norfolk	NORF	−29	168	−35.6	Auto
Okinawa	OKIN	26.7	128.2	20.2	Manual
Perth	PERT	−32	116.1	−43.2	Auto
Port Stanley	PORT	−51.6	−57.9	−39.7	Auto
Pruhonice	PRUH	50	14.6	45.5	Auto
Pt Arguello	PT_A	34.8	−120.5	40.3	Auto
Ramey	RAME	18.5	−67.1	26.1	Auto
Santa Maria	SANT	−29.7	−53.7	−22.5	Auto
Sanya	SANY	18.3	109.4	12.2	Auto
Syowa	SYOW	−69	39.6	−66.8	Manual
Townsville	TOWN	−19.6	146.9	−28.4	Auto
Wakkanai	WAKK	45.2	141.8	38.7	Manual
Wuhan	WUHA	30.5	114.4	24.9	Auto
Yamagawa	YAMA	31.2	130.6	24.7	Manual

Note. QD lat. = Quasi Dipole Latitude as of 2020.

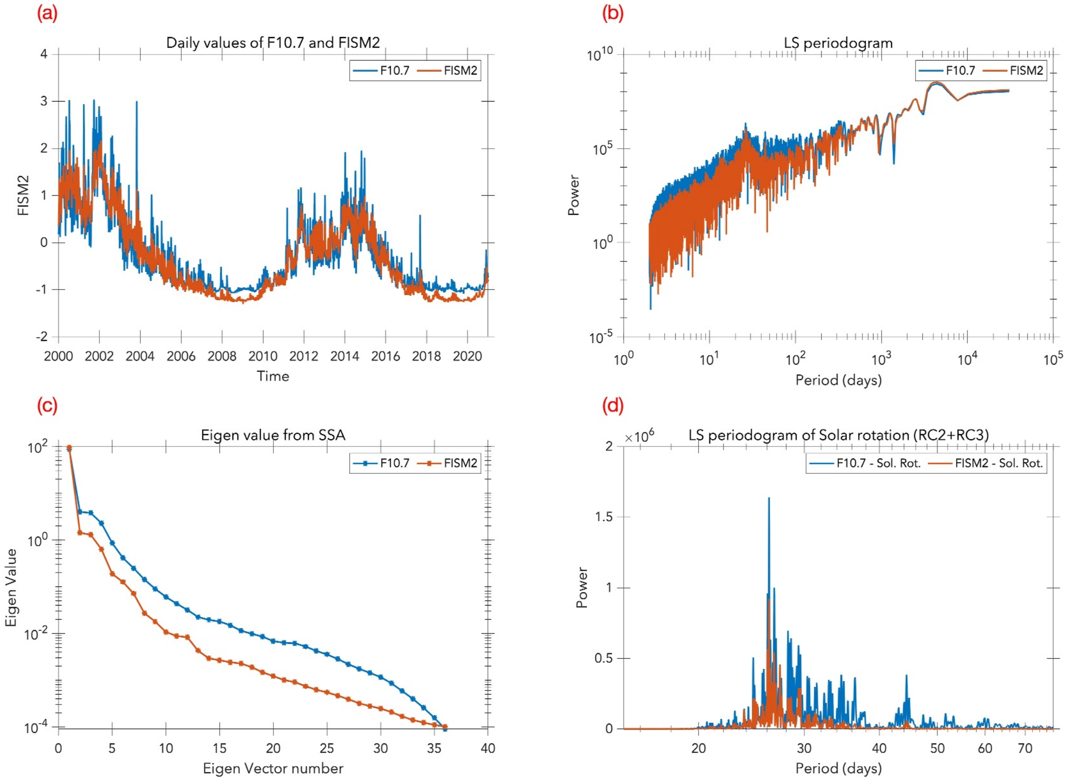

Figure 2. (a) Time series of standardized F10.7 and FISM2 (b) Lomb-Scargle periodogram of F10.7 and FISM2 (c) Eigen values from singular spectrum analysis of F10.7 and FISM2 (d) Lomb-Scargle periodogram of RC2 + RC3 for F10.7 and FISM2. See legend for line colors.

In our model equation (Equation 1), we integrate FISM2 data spanning from 0.05 to 105.05 nm, aligning with the spectral coverage of the SEE instrument on the TIMED satellite. FISM2 improves upon previous EUV models in various aspects, notably in its representation of solar rotational variations. Recently, Goncharenko et al. (2021) conducted a comparative analysis of different EUV proxies to model TEC dependence on solar irradiance, identifying FISM2 as the most effective. To assess the performance of the NmF2 model based on FISM2, we also constructed a similar model using the F10.7 index, which remains the most used solar EUV proxy in ionosphere-thermosphere models owing to its extensive historical record dating back to 1947 (Elvidge et al., 2023; Tapping, 2013 and references therein). Another proxy, the sunspot number, goes back even further in history spanning 400 years, however, it is a synthetic index that is affected by human bias and calibration (see Clette et al., 2014).

Further in this manuscript, we will use the label MF107 and MFISM to represent the local empirical models based on the F10.7 index and FISM2, respectively. Note that we do not use the modified index F10.7P in this study because we want to highlight the difference in solar rotation features in NmF2 captured by F10.7 and FISM2. Solar rotation variations in different wavelength bands stem from the uneven distribution of solar activity on the solar disk, combined with radially varying optical thickness of these emissions (Woods et al., 2005). Periodicity of solar rotation is influenced by the presence and distribution of multiple active regions on the solar disk, their positioning in solar latitude, and the solar differential rotation. The phase of solar rotation in a specific emission depends on its center-to-limb variation profile. F10.7 and FISM2 encompass distinct emission sources across different solar layers; thus, the nature of solar rotation in F10.7 and FISM2 is anticipated to be different. It is important to note here that monthly median models like IRI overlook the solar rotation related variability of NmF2, which can introduce prediction errors.

Figure 2 shows a comparison of various aspects of F10.7 and FISM2 time series. Panel (a) shows standardized F10.7 and FISM2 time series spanning from 2000 to 2022, while their Lomb-Scargle periodogram is shown in panel (b). It is clear that F10.7 exhibits stronger variations at shorter time scales. To examine the nature of solar rotation variability in two time series, singular spectrum analysis (SSA) is used to separate the non-stationary solar rotation component in each time series. SSA is a data adaptive technique which decomposes a time series into long-term trends and quasi oscillatory components without assuming a basis function (Elsner & Tsonis, 2013; Vautard et al., 1992). An oscillatory component identified by SSA appears as a pair of degenerate eigen vectors (having nearly same eigen value) (Vautard & Ghil, 1989). To select the appropriate window size for SSA, we perform SSA with varying window size around the solar rotation period until a clear eigen pair is identified. We found that for the F10.7 and FISM2 time series, a 36-day window results in a clear eigen pair. Panel (c) shows the eigen values of various modes of variability decomposed by SSA using a window size of 36 days. The pair of second and third eigen value corresponds to the solar rotation related variations (see Text S1 in Supporting Information S1). The net solar rotation component is estimated by adding the second and third reconstructed component. Panel (d) shows the Lomb-Scargle periodogram of the net solar rotation component of F10.7 and FISM2. It is notable that the solar rotation and other short-term variations are stronger in the F10.7 index.

2.3. Model Formulation

Model formulation is similar to Goncharenko et al. (2021), albeit with variation in solar flux lags. The model includes solar activity, geomagnetic activity, and intra-annual terms. Solar activity dependence of NmF2 is parametrized using the solar EUV flux and its square. Proxies used for solar EUV flux are F10.7 and FISM2 as explained in previous subsection. The influence of geomagnetic activity is defined using the ap3 index at various lags (0, 3, 6, 9, 12, 24, 48, and 72 hr). Annual and intra-annual variation of NmF2 is represented by harmonic terms up to 3rd harmonics of the day of year. Lastly, the interaction terms between the solar activity and seasonal variation are included. The mathematical expression of model is given by Equation 1.

$$\mathrm{NmF2}(t,\mathrm{DOY}) = \mathrm{NmF2}_0 + \mathrm{NmF2}_{\mathrm{solar}}(t) + \mathrm{NmF2}_{\mathrm{geomag}}(t) + \mathrm{NmF2}_{\mathrm{season}}(\mathrm{DOY}) + \mathrm{NmF2}_{\mathrm{inter}}(t,\mathrm{DOY}) \tag{1}$$

where, $\mathrm{NmF2}_0$ is the intercept term. The remaining model terms are expanded as:

$$\mathrm{NmF2}_{\mathrm{solar}}(t) = a_1 * \mathrm{EUV}(t-48) + a_2 * \mathrm{EUV}(t-48)^2$$

$$\mathrm{NmF2}_{\mathrm{geomag}}(t) = \sum_{l=0,3,9,12,24,48,72\ \mathrm{hours}} b_l * \mathrm{Ap3}(t-l)$$

$$\mathrm{NmF2}_{\mathrm{season}}(\mathrm{DOY}) = \sum_{i=1}^{3}\left(c_i \sin\frac{2i\pi * \mathrm{DOY}}{365} + d_i \cos\frac{2i\pi * \mathrm{DOY}}{365}\right)$$

$$\begin{aligned}\mathrm{NmF2}_{\mathrm{inter}}(t,\mathrm{DOY}) = {} & \mathrm{EUV}(t-48) * \sum_{j=1}^{3}\left(e_j \sin\frac{2j\pi * \mathrm{DOY}}{365} + f_j \cos\frac{2j\pi * \mathrm{DOY}}{365}\right) \\ & + \mathrm{EUV}(t-48)^2 * \sum_{k=1}^{2}\left(g_k \sin\frac{2k\pi * \mathrm{DOY}}{365} + h_k \cos\frac{2k\pi * \mathrm{DOY}}{365}\right)\end{aligned}$$

Here, EUV is the proxy for solar EUV variability, Ap3 is the geomagnetic 3-hourly ap3 index, DOY is the day of year. The coefficients a, b, c, d, e, f, g, and h are parameters to be estimated. All model coefficients are local time (LT) dependent with a time resolution of 30 min. The inclusion of the squared EUV term and its interaction with DOY aims to account for the seasonally dependent saturation of NmF2 during periods of high solar activity, as noted in prior studies (Ikubanni & Adeniyi, 2013; Ma et al., 2009). The quadratic term for solar flux is calculated after standardizing the linear solar flux term to reduce its correlation with the linear term. While this procedure significantly reduces the correlation between even and odd degree terms, there remains a significant correlation within the even or odd degree terms themselves. We refrain from including higher degree polynomial terms of solar flux to prevent overfitting, excessive model complexity, and multicollinearity. Note that the FISM2 is adjusted to a constant distance of 1 AU, therefore when using FISM2 as EUV proxy in Equation 1, the annual term also accounts for the variation in sun-earth distance. The empirical model is solved through linear regression to determine log10(NmF2).

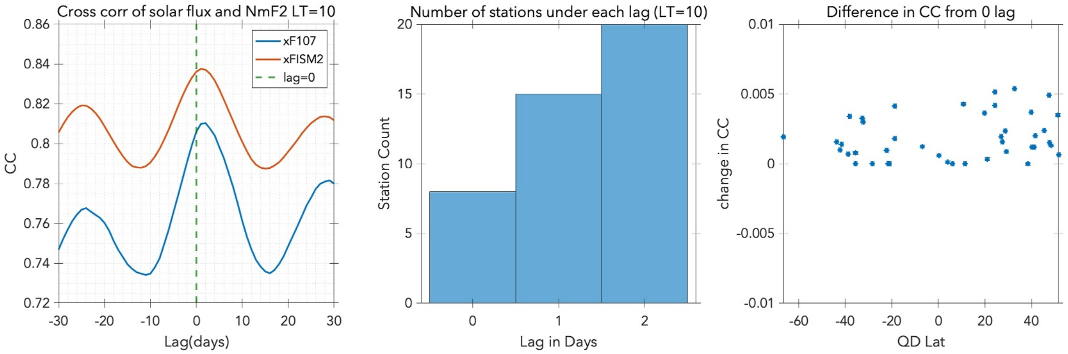

Figure 3. Correlation between solar flux and NmF2 over GRAH at LT = 10 (left). Number of stations with maximum correlation coefficient at a given lag (center). Difference between correlation coefficients at zero lag and lag of maximum correlation (right). Correlation coefficients are calculated between integrated FISM2 and NmF2 at LT = 10. Dashed green line in left panel marks the location of zero lag correlation.

The ap3 parameterization is based on Goncharenko et al. (2021). It includes multiple delays of ap3 to capture the average response to geomagnetic storms, which can persist for over 48 hr. We selected the ap3 index over the Dst index because ap3 is derived from several low- to mid-latitude stations, providing a more general proxy for solar particle flux input that affects ionospheric electron density. Borovsky and Shprits (2017) discuss the limitations of the Dst index in modeling geophysical phenomena during geomagnetic storms. The Hpo index (Yamazaki et al., 2022) with 30–60-min resolution could serve as another valuable proxy, but it only extends back to 1995 and is not suitable for modeling historical data sets.

The selection of 48-hr lag for solar EUV is based on the correlation between NmF2 and FISM2, which maximizes at a non-zero lag, as seen in Figure 3 for the GRAH station (left panel). Figure 3 also illustrates number of stations with maximum correlation at a given lag at LT = 10 (center) and difference in correlation between zero lag and lag of maximum correlation (right). Most stations have a lag of 2 days although these statistics may vary with LT. Nevertheless, the effect of lag on correlation is minimal and should not significantly affect model coefficients. It is important to note that unlike the ap3 index, we refrain from including multiple lags for solar flux proxy to prevent multicollinearity, as their time series remains highly correlated even at substantial lags.

To compare the performance of local models against the standard global empirical models, NmF2 was also computed using standard IRI-2020 model which provides two different methods for estimating NmF2/foF2: CCIR (Jones et al., 1969) and URSI (Rush et al., 1984). The IRI NmF2 used in this study is based on the URSI foF2 model plus the foF2 storm model in IRI.

3. Results and Discussion

3.1. Minimum Data Coverage to Constrain Solar Flux Dependence of NmF2

The accuracy of an empirical model of a given complexity is closely tied to the amount of training data available. Given the significant variability in data coverage of different ionosonde stations, it is important to determine the minimum number of years of data required to effectively fit/train the model in Equation 1. We use learning curves to estimate the approximate minimum data requirements. To calculate learning curve for each station, the model is trained using an increasing number of years of data until a reasonable test error is attained. Selection of training data is done in a way that mimics the real-world data coverage scenario. Initially, the training data size starts with 1 year and increments by 1 year at each training step. Each training step is repeated 30 times with data from randomly selected years. When training set spans multiple years, the first year is selected randomly and remaining years are selected consecutively to avoid sampling different parts of the solar cycle. All the remaining data, which is not used in training, is used as the test data. Training and test errors are estimated using mean squared error (MSE). Figure 4 shows the average learning curve derived from learning curves of all the ionosonde stations using F10.7 and FISM2 version of the model. It can be inferred from the learning curves that around 8 years of data coverage is required to constrain the solar flux dependence

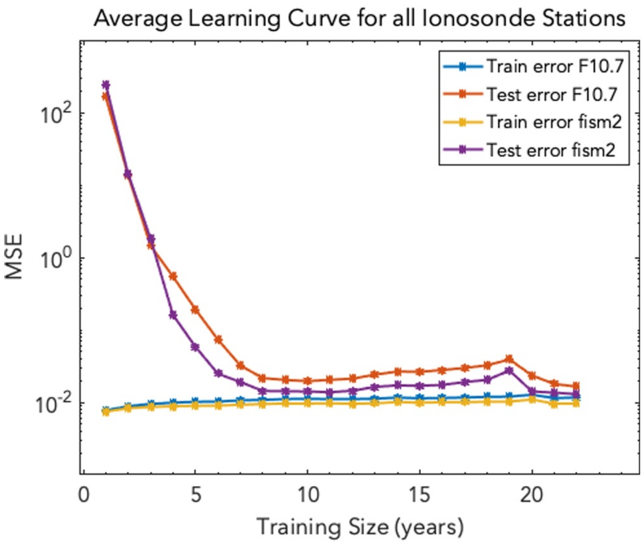

Figure 4. Learning curve of NmF2 model using F10.7 and FISM2 index. The test error saturates after 8 years of data availability.

of NmF2 using model of complexity given by Equation 1. It is worth noting here that the MSE for FISM2 model is always smaller than the F10.7 model.

3.2. Global Ionosphere Anomalies

Ionospheric anomaly term is used to mark the significant deviation of spatio-temporal behavior of the F2 layer from the Chapman ionization theory. To show that the local models capture the well-known global ionospheric anomalies, model output for all the stations at fixed low solar (F10.7 = 100) and geomagnetic (ap3 = 3) activity is binned in magnetic latitude. Figure 5 shows the variation of binned NmF2 with magnetic latitude and solar local time. Panel (a), (b), (c), and (d) corresponds to March, June, September, and December, respectively. Several ionosphere anomalies identified in Figure 5 are:

(a) Double-crest equatorial ionization anomaly (EIA) formation is seen during all the seasons (e.g., Anderson, 1981; Moffett, 1979; Raghavarao et al., 1988; Rajaram, 1977; Walker, 1981).
(b) Winter/seasonal anomaly marked by enhanced winter hemisphere NmF2 during solstice before 12 LT (Johnson, 1964; Rishbeth & Setty, 1961). Note that the winter anomaly is stronger in the northern hemisphere (Burns et al., 2014; Torr & Torr, 1973).
(c) Semiannual anomaly marked by equinox NmF2 greater than solstice (e.g., Mayr & Mahajan, 1971; Millward et al., 1996; Volland, 1969).

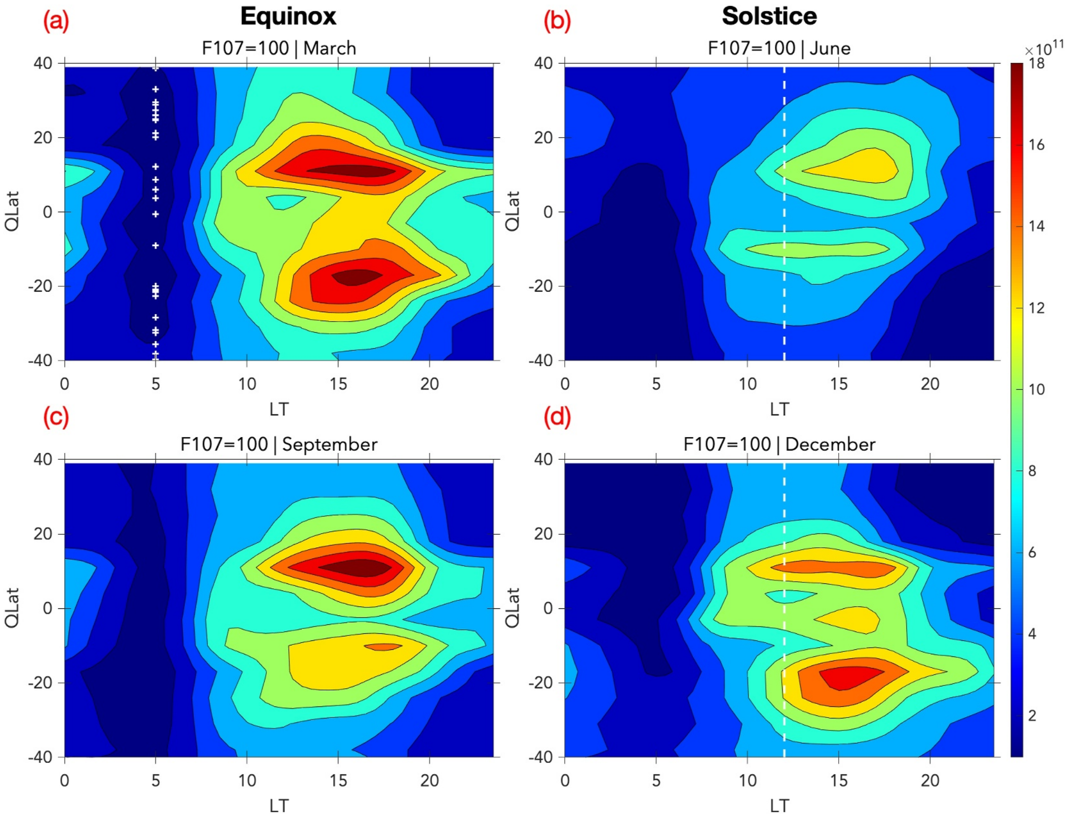

Figure 5. NmF2 model output from all stations binned in Quasi-dipole latitude and LT for (a) March, (b) June, (c) September, and (d) December at fixed F10.7 = 100 and Ap3 = 3. "+" markers in panel (a) mark the Quasi-dipole latitude of the ionosonde stations used in binning. Dashed white lines in panels (b) and (d) mark 12 LT.

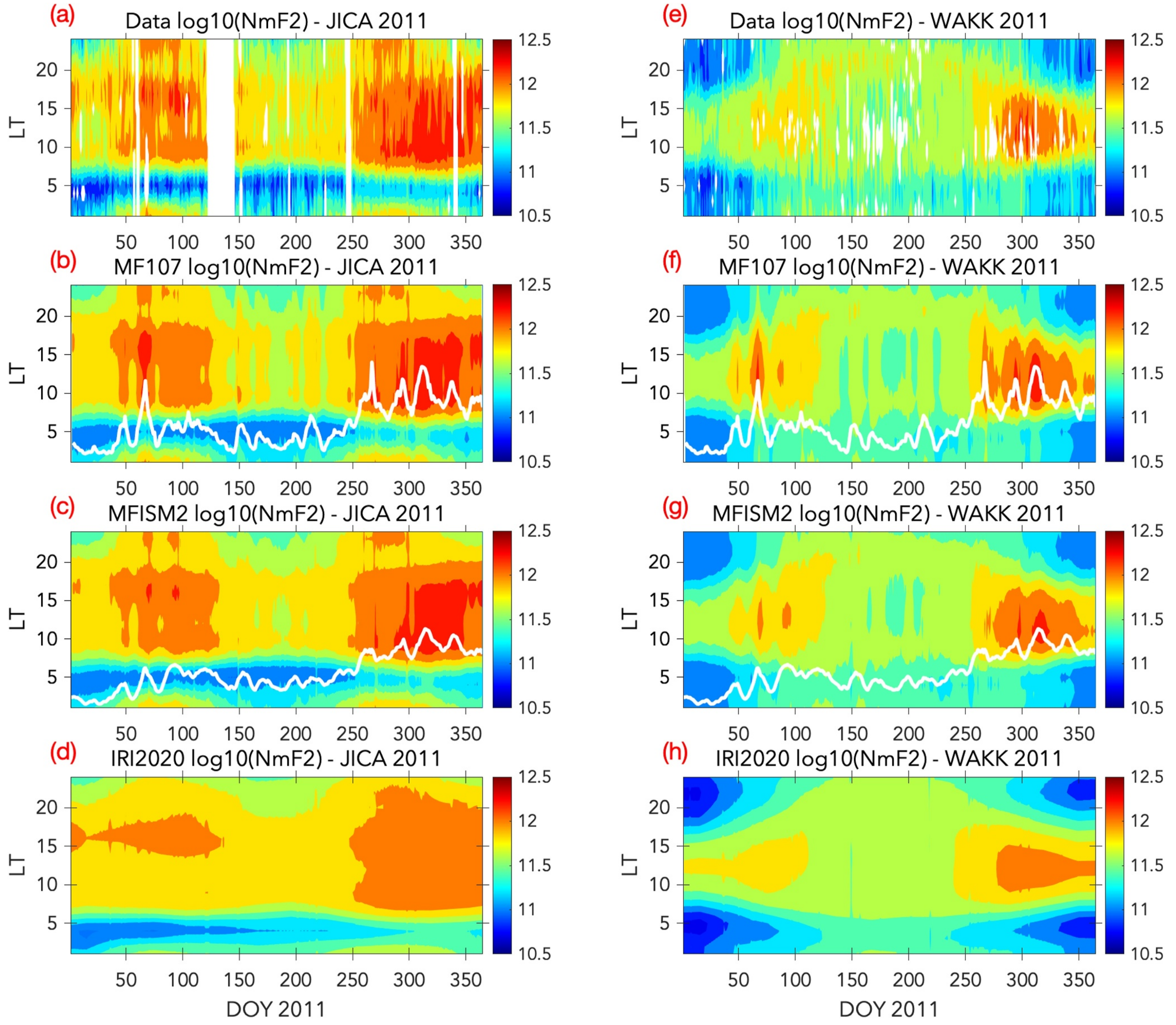

Figure 6. log10(NmF2) from Jicamarca ionosonde observation during the year 2011 (a). Prediction using NmF2 model with F10.7 (b), FISM2 (c), and IRI-2020 (d). White line in (b) and (c) indicates the F10.7 and FISM2 index, respectively. The right column is the same but for WAKK station.

(d) Annual anomaly (non-seasonal or annual asymmetry) marked by NmF2 in December solstice larger than June solstice (Berkner & Wells, 1938; Rishbeth & Muller-Wodarg, 2006; Sai Gowtam & Tulasi Ram, 2017; Yonezawa, 1971).

(e) March equinox NmF2 is greater than September equinox (Liu et al., 2010).

3.3. Model Performance Metrics

Figure 6 compares the data and model prediction for a low-latitude station Jicamarca (JICA) and mid-latitude station Wakkanai (WAKK) for the year 2011. Both MFISM and MF107 capture the solar flux, seasonal and LT variation of NmF2, with MFISM generally closer to the observations. IRI-2020 underestimates NmF2, especially at JICA location. IRI-2020 also does not properly capture several prominent features in seasonal and LT variations at WAKK; it misses morning and evening peaks in NmF2 during summer season, overestimates noontime NmF2 in winter and underestimates nighttime NmF2 in winter. Also note that solar rotation signal is larger in F10.7 and MF107 NmF2. MF107 overpredicts NmF2 response to solar rotation in comparison with

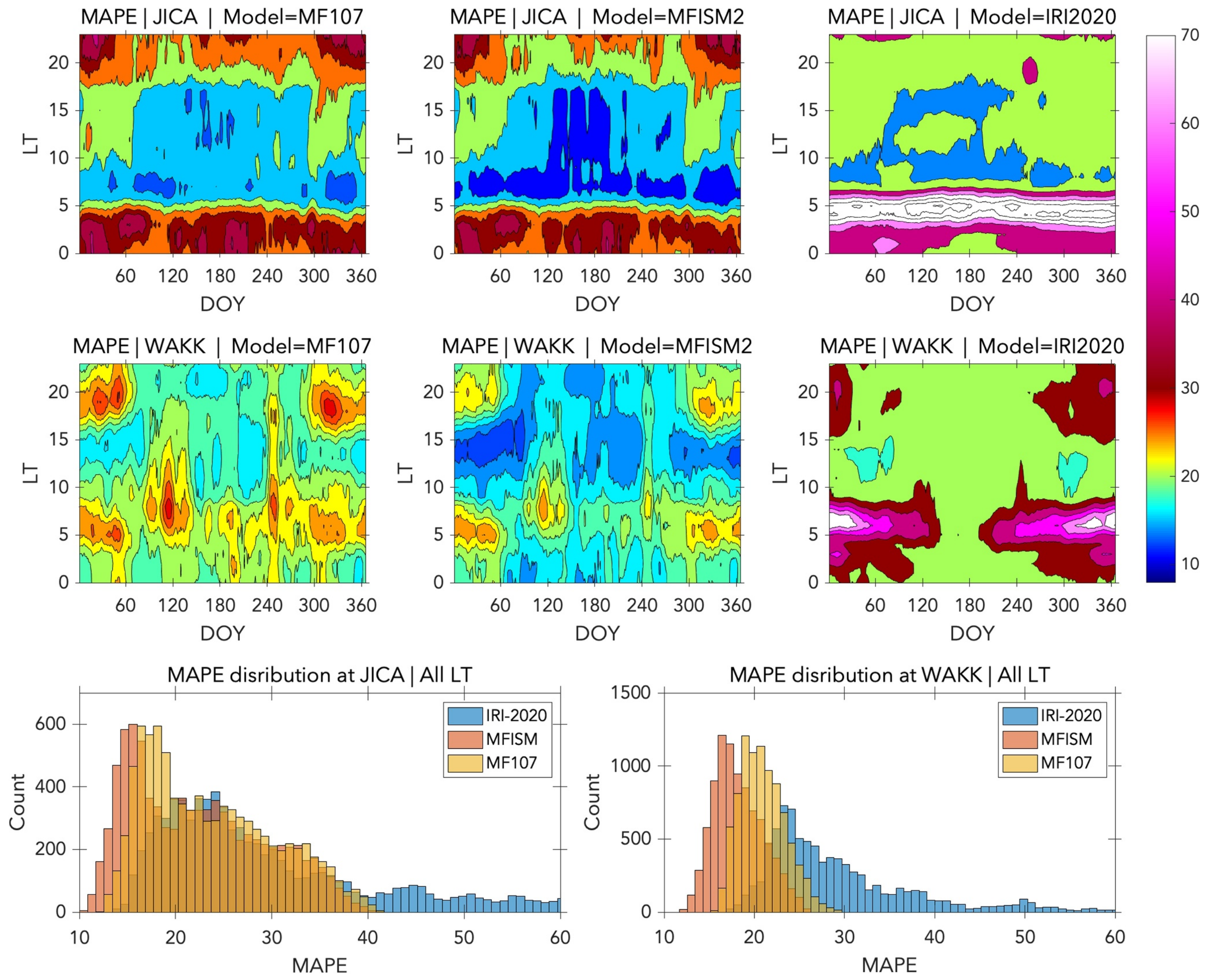

Figure 7. MAPE for JICA (top) and WAKK (center) models. Left, center and right panels correspond to MF107, MFISM and IRI2020, respectively. Bottom panel shows the distribution of MAPE for JICA (left) and WAKK (right) station across all LTs. Colorbar is stretched to show IRI-2020 errors.

observations for both stations. A more comprehensive discussion about solar rotation signal in MF107 and MFISM is provided in Section 3.5.

We utilized several metrics to examine performance of models in a comprehensive manner (Liemohn et al., 2021). Figure 7 shows the LT and seasonal variation of MAPE (mean absolute percentage error) for MF107, MFISM, and IRI-2020 models over JICA and WAKK stations, considering data from all the years within their coverage period. During the daytime, MFISM shows a noticeable improvement over MF107 and IRI-2020 at both the stations. However, for the JICA station, there are larger nighttime errors in MF107 and MFISM. The discrepancy might be attributed to the independent modeling of NmF2 at each LT. Notably, this discrepancy is absent at the WAKK station. WAKK station generally has larger MAPE in winter during the morning and evening time. IRI MAPE is exceptionally large during morning time at both the stations. The bottom panel shows the distribution of MAPE for JICA and WAKK station across all the LTs and summarizes the conclusion that FISM2-driven model provides most accurate description of NmF2.

Figure 8 shows the RMSE (root mean square error) and MAPE for three models and all stations as a function of magnetic latitude and season at 13 LT. MFISM (first panel) has the lowest RMSE and MAPE among the three models. Both RMSE and MAPE are larger in the northern hemisphere than the southern hemisphere. One of the potential reasons for larger errors in the northern hemisphere could be the atmospheric forcing at northern EIA

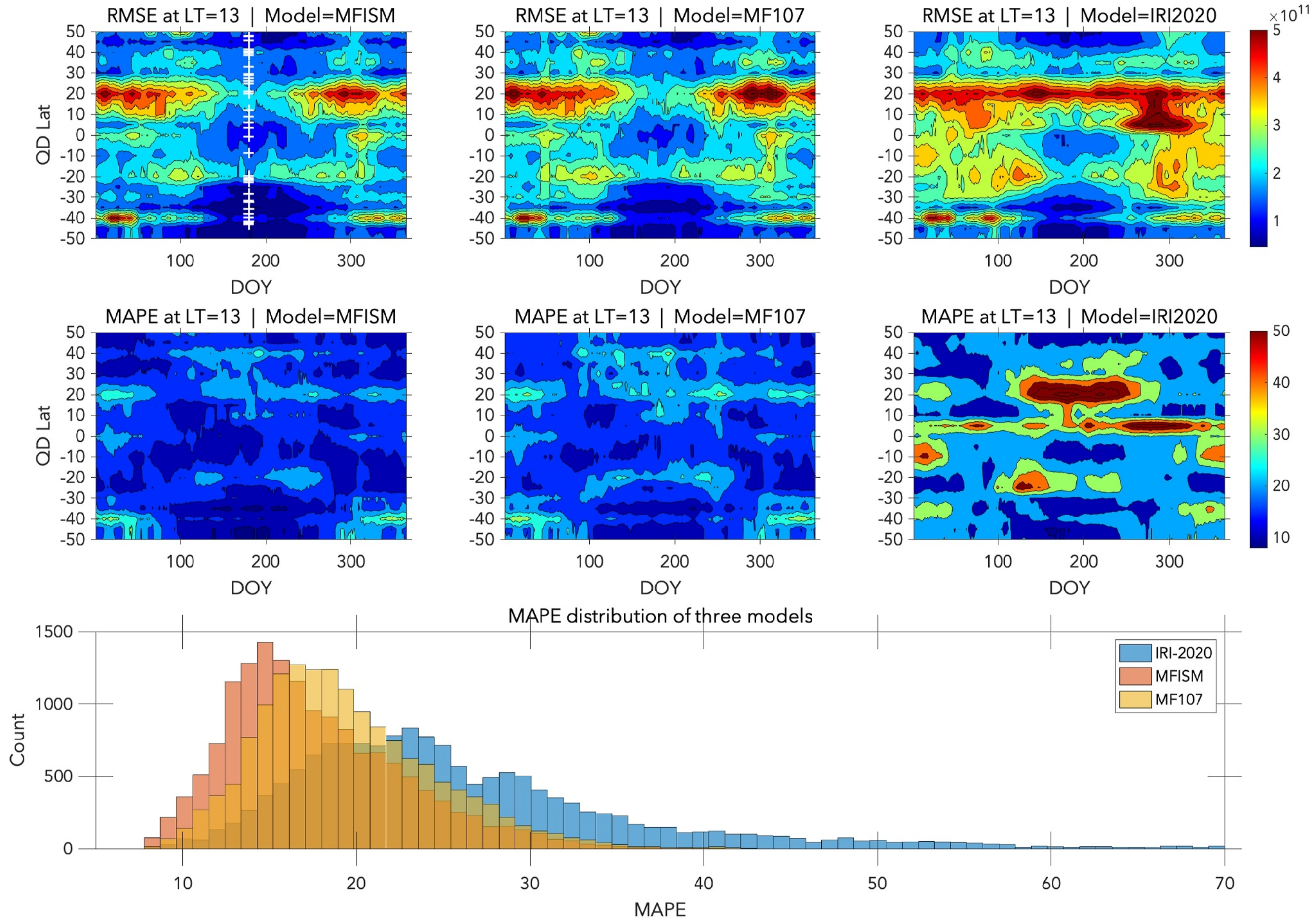

Figure 8. RMSE (top) and MAPE (mid) for MFISM (left), MF107 (center), and IRI-2020 (right) models. Interpolated in QD latitude. White markers in first panel at DOY = 180 marks the location of stations in QD latitude used for interpolation. Bottom panel shows the histogram of MAPE for each model.

latitudes. However, the latitude dependence of error needs to be interpreted with caution because it is biased by the data availability at a given station and solar cycle coverage. Of the three models, IRI-2020 has the largest error partly due to the unresolved solar rotation. For IRI-2020, the latitudes with worst errors are contributed by GUAM, SANT, and OKIN stations where MAPE reaches 70% during some months (note that the colorbar is saturated). Error at SANT station is biased toward the low solar activity due to biased data coverage (not shown). As we will see in further sections, IRI-2020 tends to overestimate NmF2 at low solar activity and hence have larger errors. OKIN on the other hand has extensive data coverage for over 50 years, so the error cannot be attributed to a specific solar activity. For MFISM and MF107, latitudes with largest errors are due to NIUE, DARW, COCO, LUAL, and DYES stations; all these stations have less than 8 years of data coverage. MAPE for these stations gets as large as 35% during certain seasons. MFISM has the lowest MAPE among these models which stays around 15% for the stations with good data coverage (see bottom panel).

The performance of MFISM and MF107 at different solar activity levels, seasons and LTs can be compared by using skill score. Skill score enables the comparison of different metrics between two model versions (Liemohn et al., 2021; Murphy, 1988). Skill score for mean square error (MSE) accuracy metrics is given as

$$\mathrm{SS}_{\mathrm{MSE}} = 1 - \frac{\sum\left(M_i^{\mathrm{FISM}} - O_i\right)^2}{\sum\left(M_i^{F107} - O_i\right)^2}$$

A positive (negative) skill score indicates the newer model version is better (worse) than the previous version. Figure 9 shows the skill score for MF107 and MFISM comparison at low (top), moderate (middle) and high

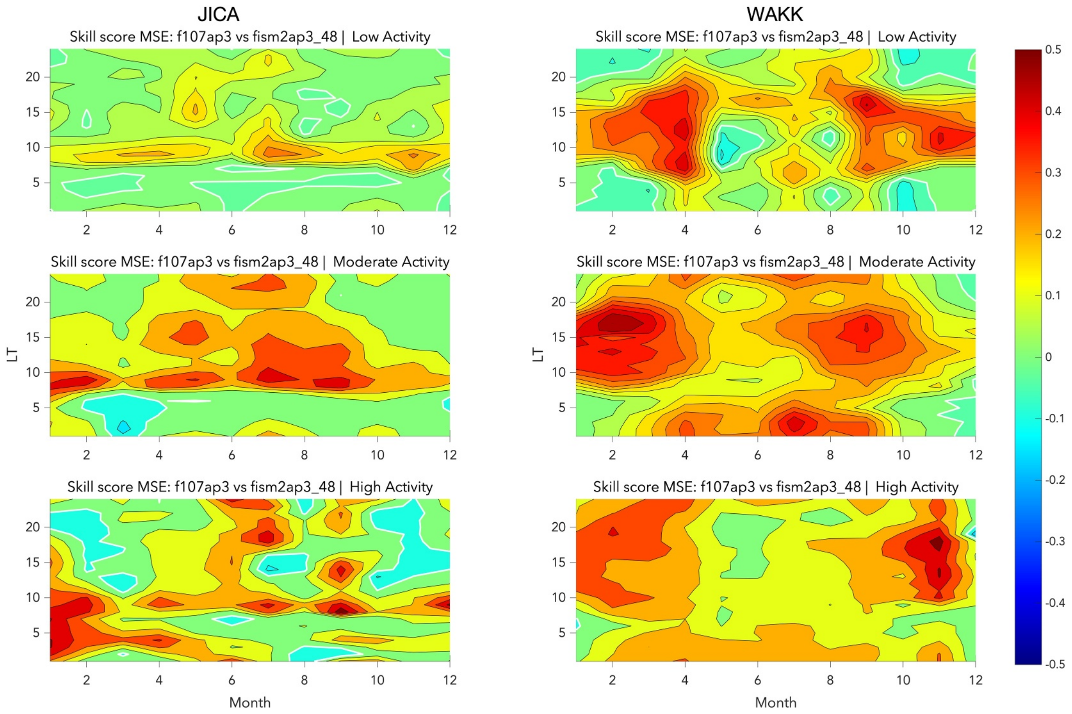

Figure 9. Comparison of Skill score between model with F10.7 and FISM2 over Jicamarca (left panel) and Wakkanai (right panel). Top, middle, and bottom panels correspond to low, medium, and high solar activity, respectively. Positive values indicate model with FISM2 performs better than model with F10.7 and vice versa. Bold white lines envelope the regions with negative skill score.

(bottom) solar activity for JICA (left) and WAKK (right). The low, moderate, and high solar activity is defined as 0–25, 25–75 and 75–100 percentile of the available FISM2 values. It is clear that MFISM always performs better than MF107 at all solar activity levels. The skill score and accuracy discussed in this, and the previous sub-section does not give insights on the subtle differences between these models. The following sub-sections focus on the nature of difference between these models.

3.4. Performance at Solar Maxima and Minima

Previous research has shown that the decline in F10.7 during the deep solar minima of 2008 does not align proportionally with EUV (Chen et al., 2011). This observation is confirmed by the MF107 prediction for KOKU station in Figure 10. The top panel of the figure displays box plots of data, MFISM, MF107, and IRI-2020 predictions at 13 LT across various solar minima. Here the solar minima data refers to the period 1 year before and after FISM2 reaches its minimum value during each solar minimum. The bottom panel illustrates the time series of KOKU data and model predictions during the 2008 minimum. Notably, during the 2008 and 2019 minima, MF107 tends to overestimate NmF2. MFISM also overestimates NmF2 but to a lesser degree. Conversely, IRI-2020 consistently overestimates NmF2 during all solar minima. Lühr and Xiong (2010) reported from CHAMP observations that IRI-2007 overestimated ionospheric electron density during 2008–2009 by 50%–60%. This problem also persisted in IRI-2012 where it cannot reproduce the reduction in NmF2 during the deep solar minima of 2008–2009 (Ezquer et al., 2014; Perna et al., 2017). Perna et al. (2017) reported that IRI performs better at mid latitudes than low latitudes during the solar minima. It's worth noting here that we did not observe IRI-2020 overestimation at WAKK which is a mid-latitude station (see also Araujo-Pradere et al., 2011). Overall, the local empirical models MF107 and MFISM offer more accurate estimation of NmF2 during solar minima, and MFISM is the most accurate among these models.

Figure 11 illustrates the performance of various models during solar maxima at 13 LT over KOKU. The top panel displays box plots of data and model predictions across different solar maxima, while the bottom panel shows the time series of these models during the 2001 solar maximum. It's evident from the figure that IRI-2020

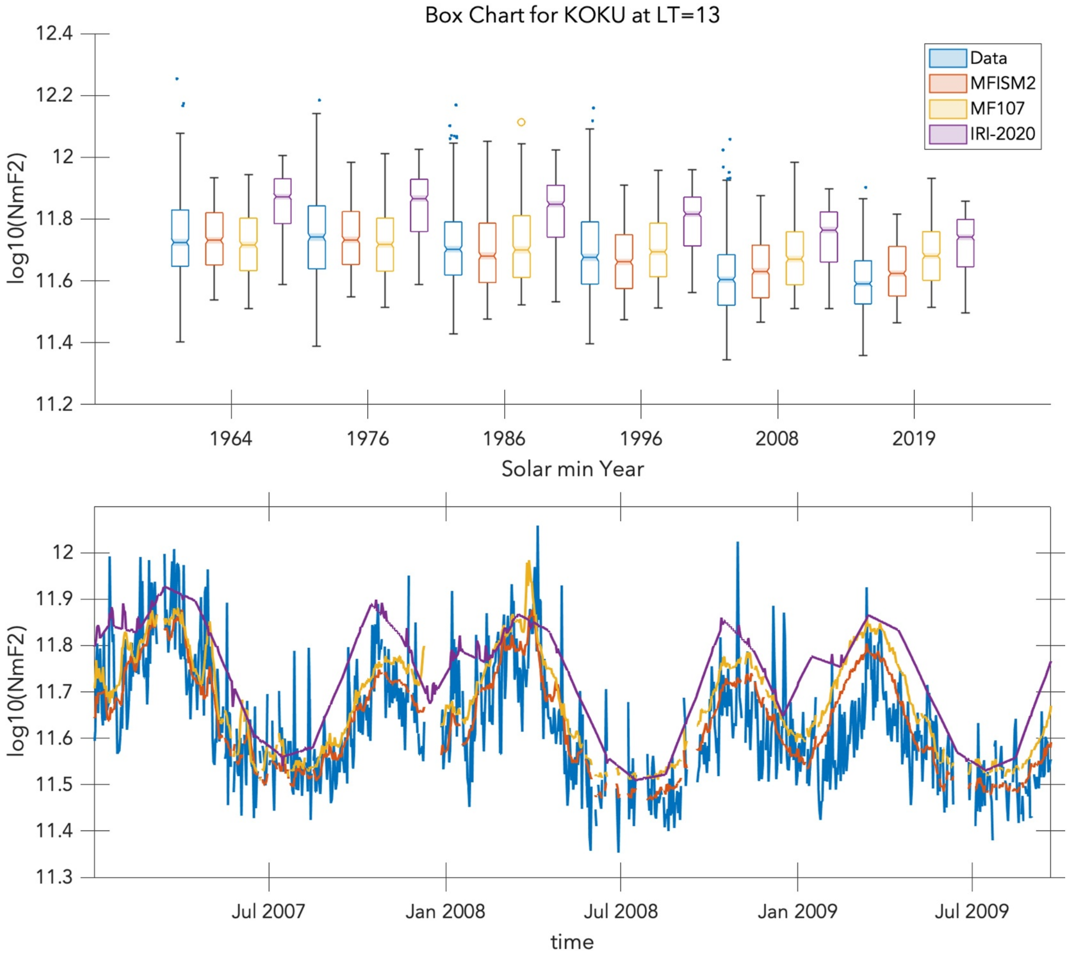

Figure 10. Top panel shows the box plot of KOKU data (blue), MFISM (red), MF107 (yellow), and IRI-2020 (violet) at 13 LT during the years of solar minima. Bottom plot shows the time series of log10(NmF2) at 13 LT for all the models during 2008–2009 solar minima.

consistently overestimates NmF2 during all solar maxima. Further, the time series in the bottom panel indicates that IRI-2020's overestimation becomes most pronounced during the summer months, a pattern observed at other stations as well (not shown). Both MF107 and MFISM offer improved predictions over IRI-2020.

Summarizing the model performance during solar maxima and minima (via box plots and time series plots), it can be inferred that during solar minima, IRI-2020 tends to overestimate NmF2 across all seasons. Conversely, during solar maxima, IRI-2020 overestimates NmF2 particularly in the summer season. MFISM exhibits the least overestimation. The variance in performance between MF107 and MFISM at solar extrema is attributed to non-linearity in the relationship between F10.7 and solar EUV irradiance.

3.5. Solar Rotation Features in NmF2 Data and Model

This section discusses only the MF107 and MFISM models because IRI does not resolve solar rotation features in NmF2. To quantify the solar rotation predicted by these models, we use SSA to resolve the quasi-oscillatory modes corresponding to the solar rotation. The eigen values of these modes are used to express the strength of solar rotation at each station and model. Similar to Section 2.2, the selection of window size for SSA is based on the eigen pair formation. It was found that a window size of 47 and 43 days resulted in clear eigen pair formation for the data and model time series, respectively. Panel (a) of Figure 12 shows the eigen modes corresponding to solar rotation in NmF2 data, MF107, and MFISM for JICA station at 13 LT. Panel (b) shows the eigen values of different modes in the three time series. The degenerative eigen value pair of 3rd and 4th eigen value corresponds to the solar rotation mode. These eigen values suggest that the variance explained by the solar rotation in NmF2

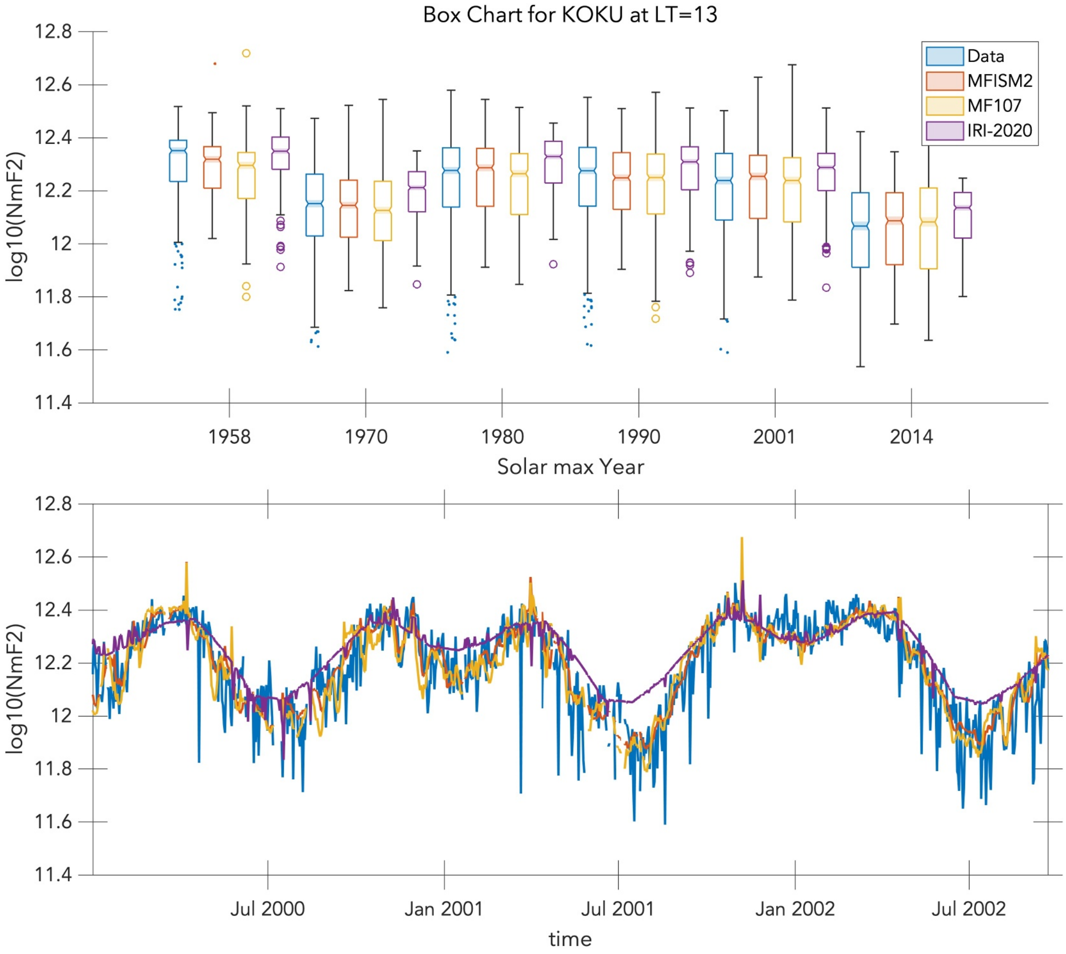

Figure 11. Same as Figure 10 but for solar maxima.

data, F10.7 model and FISM2 model is 2.04%, 6%, and 2.41%, respectively. Panel (c) shows the periodogram of reconstructed solar rotation modes in each time series for JICA station. It can be inferred from panel (b) and (c) that the solar rotation variance and periodicity in MFISM is more similar to data as compared to MF107 and that MF107 always overemphasizes strength and periods of solar rotation. Panel (d) shows the eigen value of solar rotation component predicted by MF107 and MFISM at various stations against their magnetic latitude. It is clear that MF107 overestimates the solar rotation variance for all the stations.

One of the reasons for discrepancy in solar rotation between MFISM and MF107 is the contribution of optically thick coronal gyroresonance to F10.7. Schonfeld et al. (2019) reported that the solar rotation variability in F10.7 is often driven by the discrete gyroresonance sources on solar disk which is unrelated to the EUV emissions. The discrepancy between solar rotation in MFISM and data is relatively small and might be partly attributed to the use of integrated FISM2 in the present study. This is because the solar rotation variability is different in different EUV bands (Chamberlin et al., 2007).

4. Summary

Empirical models of the ionosphere play a vital role in our increasingly space weather-aware society. With a shift in focus from ionospheric climate to ionospheric weather, these models must expand beyond their traditional monthly median predictions. This necessitates the availability of suitable EUV proxies or models capable of capturing the solar irradiance dependence of NmF2 on shorter time scales. In this study, we examined the efficacy of local empirical models, based on 43 low to mid-latitude ionosondes, in capturing the day-to-day variability of NmF2 related to solar irradiance. The first model relies on the F10.7 index, traditionally used as an EUV proxy,

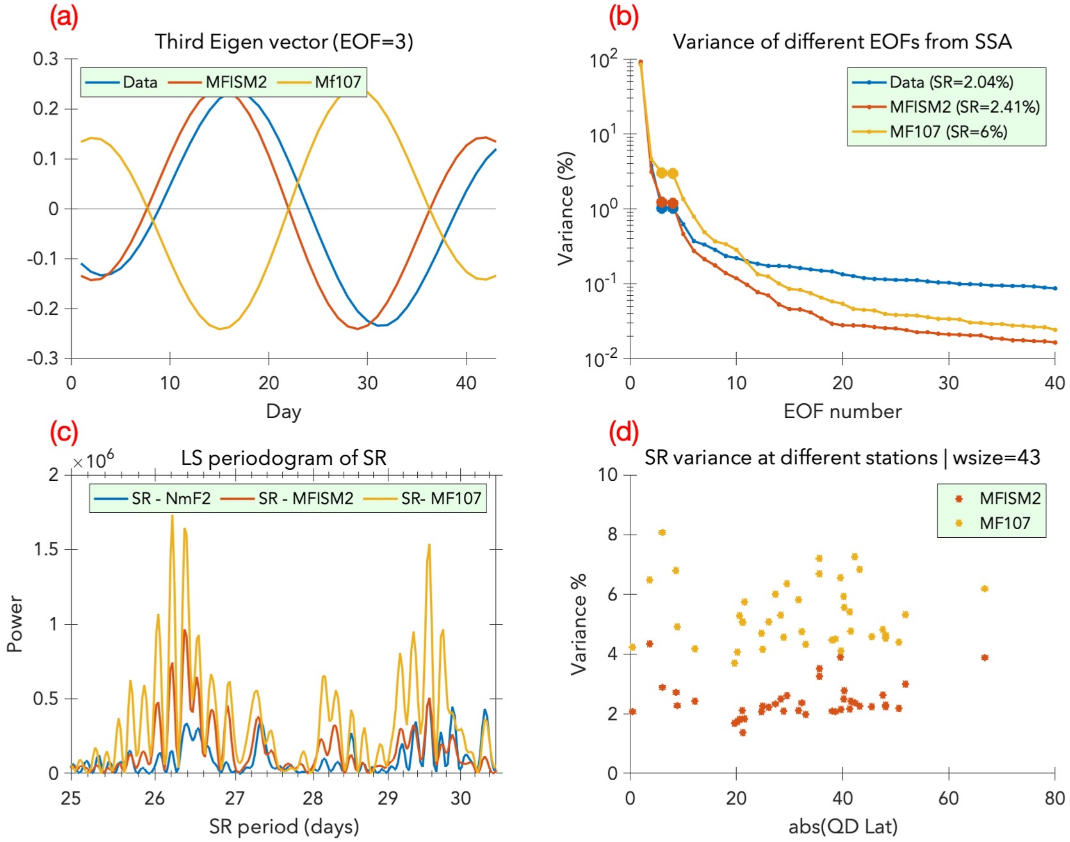

Figure 12. (a) Third EOF from SSA of data, MF107 prediction and MFISM prediction for JICA at LT = 13. (b) Eigen values (in units of percentage variance) of different EOFs from SSA with window size = 47 for data and 43 for model prediction. Three lines correspond JICA ionosonde NmF2, MF107, and M FISM2. (c) Lomb-Scargle periodogram of the solar rotation component (sum of RCs corresponding to eigen pairs in (b)). (d) Combined variance (%) of RC3 and RC4 from MFISM and MF107 at different stations as a function of QD latitude. See legend for color codes (SR = Solar rotation).

while the second model is based on the FISM2, empirical model of solar irradiance based on observations from multiple satellite missions. We also compared the predictive performance of these models against the IRI-2020 model. Key findings from this study include:

- Approximately 8 years of data coverage is necessary to effectively capture the solar flux dependence of NmF2.
- The combined output of local NmF2 models accurately reflects well-known global ionospheric anomalies. Local empirical models demonstrate lower prediction errors compared to the IRI-2020 model across all stations, with some locations showing significantly superior performance.
- FISM2-driven models exhibit superior predictive capabilities for NmF2 compared to F10.7-driven models. One of the reasons for the enhanced performance of FISM2-driven models is their accuracy in predicting the strength of solar rotation in NmF2. Additionally, FISM2-driven models perform better in predicting NmF2 during the solar minima and maxima. The Mean Absolute Percentage Error (MAPE) for the FISM2-based models is typically around 15%.
- MF10.7 overestimates NmF2 during the 2008 and 2019 solar minima.
- IRI-2020 overestimates NmF2 during all solar maxima and minima. Overestimation during solar maxima is increased during the summer months.

Earlier, Goncharenko et al. (2021) concluded that FISM2-driven model outperforms models driven by other solar activity indices or proxies for empirical modeling of TEC at middle latitude. Combination of these results suggests that FISM2 is the most suitable solar activity proxy for empirical modeling of ionospheric electron density.

The findings presented here demonstrate significant benefit to the ionospheric research community from implementing advances obtained by the solar physics community. In particular, accurate description of solar spectral irradiance variability that is provided by FISM2 and enabled by TIMED/SEE, SORCE/SOLSTICE, SDO/EVE, and other missions, is an important component in better understanding and prediction of ionospheric parameters. As solar EUV is a major driver of ionospheric and thermospheric variability on both short-term and long-term scales, these results have implications for space weather studies and development of more accurate ionospheric models that meet demands of modern technological society.

Some findings from the current study bear significant implications for understanding the influence of lower atmospheric forcing and long-term trends in the ionosphere. While extensive data coverage may not be essential for developing empirical models in this study, it is crucial for quantifying the ionosphere's long-term variations in response to interannual changes in atmospheric forcing and geomagnetic secular variation. Further, the accountability of solar rotation in NmF2 variability could also be a crucial factor in diagnosing atmospheric forcing effects on the F region ionosphere. The unaccounted solar rotational signal can be misinterpreted as due to atmospheric forcing. Future iterations of these models will incorporate considerations for geomagnetic secular variations and lunar tide-related variations in NmF2, which is expected to further enhance the accuracy of NmF2 predictions and will allow to resolve lower atmospheric forcing and long-term trends in the F region ionosphere.

Data Availability Statement

Auto-scaled ionosonde data used in this study is retrieved from Lowell GIRO Data Center (GIRO, 2011; Reinisch & Galkin, 2011). Manually scaled ionosonde data is provided by WDC for Ionosphere and Space Weather, Tokyo, National Institute of Information and Communications Technology (WDC for Ionosphere and Space Weather, n.d.). Daily averaged EUV flux from FISM2 is available from LASP Interactive Solar Irradiance Datacenter (Chamberlin et al., 2020; LISIRD, 2005). F10.7 and ap3 index are available from Madrigal Database (CEDAR Madrigal database geoindices, 1950). Model coefficients and forward code for the regional NmF2 empirical models are archived at https://doi.org/10.5281/zenodo.13242667 (Singh & Goncharenko, 2024).

Acknowledgments

This research draws upon data provided by the Lowell Global Ionosphere Radio Observatory (GIRO) Data Center and WDC for Ionosphere and Space Weather, Tokyo, National Institute of Information and Communications Technology (NICT). Information about GIRO data resources is available at http://spase.info/SMWG/Observatory/GIRO. MIT Haystack Observatory effort is supported by NASA Grant 80NSSC22K1074, NSF Grant AGS-1952737, ONR Grant N00014-24-1-2122, and NSF Grant AGS-2411430. F. Redondo was supported by the NSF Research Experience for Undergraduates Grant AST-1950348 for his internship at MIT Haystack Observatory in summer 2023. P. Chamberlin acknowledges support through NASA Grant 80NSSC23K0902.

References

Anderson, D. N. (1981). Modeling the ambient, low-latitude, F region ionosphere: A review. *Journal of Atmospheric and Terrestrial Physics*, *43*(8), 753–762. https://doi.org/10.1016/0021-9169(81)90051-9

Araujo-Pradere, E. A., Redmon, R., Fedrizzi, M., Viereck, R., & Fuller-Rowell, T. J. (2011). Some characteristics of the ionospheric behavior during the solar cycle 23–24 minimum. *Solar Physics*, *274*(1–2), 439–456. https://doi.org/10.1007/s11207-011-9728-3

Balan, N., Bailey, G. J., Jenkins, B., Rao, P. B., & Moffett, R. J. (1994). Variations of ionospheric ionization and related solar fluxes during an intense solar cycle. *Journal of Geophysical Research*, *99*(A2), 2243–2253. https://doi.org/10.1029/93JA02099

BenMoussa, A., Gissot, S., Schühle, U., Del Zanna, G., Auchère, F., Mekaoui, S., et al. (2013). On-orbit degradation of solar instruments. *Solar Physics*, *288*(1), 389–434. https://doi.org/10.1007/s11207-013-0290-z

Berkner, L. V., & Wells, H. W. (1938). Non-seasonal change of F2-region ion density. *Terrestrial Magnetism and Atmospheric Electricity*, *43*(1), 15–36. https://doi.org/10.1029/TE043i001p00015

Bilitza, D., Pezzopane, M., Truhlik, V., Altadill, D., Reinisch, B. W., & Pignalberi, A. (2022). The International Reference Ionosphere model: A review and description of an ionospheric benchmark. *Reviews of Geophysics*, *60*(4), e2022RG000792. https://doi.org/10.1029/2022RG000792

Borovsky, J. E., & Shprits, Y. Y. (2017). Is the Dst index sufficient to define all geospace storms? *Journal of Geophysical Research: Space Physics*, *122*(11), 11–543. https://doi.org/10.1002/2017ja024679

Burns, A. G., Wang, W., Qian, L., Solomon, S. C., Zhang, Y., Paxton, L. J., & Yue, X. (2014). On the solar cycle variation of the winter anomaly. *Journal of Geophysical Research: Space Physics*, *119*(6), 4938–4949. https://doi.org/10.1002/2013JA019552

Cander, L. R. (2019). Ionosphere space weather and radio propagation. In *Ionospheric space weather*. *Springer geophysics*. Springer. https://doi.org/10.1007/978-3-319-99331-7_8

CEDAR Madrigal database geoindices. (1950). Geoindices [Dataset]. CEDAR Madrigal distributed database at MIT Haystack Observatory. Retrieved from https://w3id.org/cedar?experiment_list=experiments/1950/gpi/01jan50&file_list=geo500101g.002.hdf5

Cessateur, G., Lilensten, J., de Wit, T. D., BenMoussa, A., & Kretzschmar, M. (2012). New observation strategies for the solar UV spectral irradiance. *Journal of Space Weather and Space Climate*, *2*, A16. https://doi.org/10.1051/swsc/2012016

Chamberlin, P. C., Eparvier, F. G., Knoer, V., Leise, H., Pankratz, A., Snow, M., et al. (2020). The flare irradiance spectral model-version 2 (FISM2). *Space Weather*, *18*(12), e2020SW002588. https://doi.org/10.1029/2020SW002588

Chamberlin, P. C., Woods, T. N., & Eparvier, F. G. (2007). Flare irradiance spectral model (FISM): Daily component algorithms and results. *Space Weather*, *5*(7), S07005. https://doi.org/10.1029/2007SW000316

Chartier, A. T., Steele, J., Sugar, G., Themens, D. R., Vines, S. K., & Huba, J. D. (2023). Validating ionospheric models against technologically relevant metrics. *Space Weather*, *21*(12), e2023SW003590. https://doi.org/10.1029/2023SW003590

Chen, Y., Liu, L., & Wan, W. (2011). Does the F10. 7 index correctly describe solar EUV flux during the deep solar minimum of 2007–2009? *Journal of Geophysical Research*, *116*(A4), A04304. https://doi.org/10.1029/2010JA016301

Clette, F., Svalgaard, L., Vaquero, J. M., & Cliver, E. W. (2014). Revisiting the sunspot number: A 400-year perspective on the solar cycle. *Space Science Reviews*, *186*(1–4), 35–103. https://doi.org/10.1007/s11214-014-0074-2

De Gasperin, F., Mevius, M., Rafferty, D. A., Intema, H. T., & Fallows, R. A. (2018). The effect of the ionosphere on ultra-low-frequency radio-interferometric observations. *Astronomy & Astrophysics*, *615*, A179. https://doi.org/10.1051/0004-6361/201833012

de Wit, T. D., Kretzschmar, M., Aboudarham, J., Amblard, P. O., Auchère, F., & Lilensten, J. (2008). Which solar EUV indices are best for reconstructing the solar EUV irradiance? *Advances in Space Research*, *42*(5), 903–911. https://doi.org/10.1016/j.asr.2007.04.019

Donnelly, R. F. (1987). Gaps between solar UV & EUV radiometry and atmospheric sciences. In P. Foukal (Ed.), *Solar radiative output variation* (p. 139). Cambridge Research & Instrumentation, Inc.

Donnelly, R. F., Heath, D. F., Lean, J. L., & Rottman, G. J. (1983). Differences in the temporal variations of solar UV flux, 10.7-cm solar radio flux, sunspot number, and Ca-K plage data caused by solar rotation and active region evolution. *Journal of Geophysical Research*, *88*(A12), 9883–9888. https://doi.org/10.1029/JA088iA12p09883

Elsner, J. B., & Tsonis, A. A. (2013). *Singular spectrum analysis: A new tool in time series analysis*. Springer Science & Business Media. https://doi.org/10.1007/978-1-4757-2514-8

Elvidge, S., Themens, D. R., Brown, M. K., & Donegan-Lawley, E. (2023). What to do when the F10.7 goes out? *Space Weather*, *21*(4), e2022SW003392. https://doi.org/10.1029/2022SW003392

Ezquer, R. G., López, J. L., Scidá, L. A., Cabrera, M. A., Zolesi, B., Bianchi, C., et al. (2014). Behaviour of ionospheric magnitudes of F2 region over Tucumán during a deep solar minimum and comparison with the IRI 2012 model predictions. *Journal of Atmospheric and Solar-Terrestrial Physics*, *107*, 89–98. https://doi.org/10.1016/j.jastp.2013.11.010

GIRO. (2011). Autoscaled ionosonde data [Dataset]. Digital ionogram database of Global Ionospheric Radio Observatory (GIRO) at University of Massachusetts Lowell. Retrieved from https://giro.uml.edu/didbase/scaled.php

Goncharenko, L. P., Tamburri, C. A., Tobiska, W. K., Schonfeld, S. J., Chamberlin, P. C., Woods, T. N., et al. (2021). A new model for ionospheric total electron content: The impact of solar flux proxies and indices. *Journal of Geophysical Research: Space Physics*, *126*(2), e2020JA028466. https://doi.org/10.1029/2020JA028466

Hinteregger, H. E. (1981). Representations of solar EUV fluxes for aeronomical applications. *Advances in Space Research*, *1*(12), 39–52. https://doi.org/10.1016/0273-1177(81)90416-6

Hinteregger, H. E., Fukui, K., & Gilson, B. R. (1981). Observational, reference and model data on solar EUV, from measurements on AE-E. *Geophysical Research Letters*, *8*(11), 1147–1150. https://doi.org/10.1029/GL008i011p01147

Ikubanni, S. O., & Adeniyi, J. O. (2013). Variation of saturation effect in the ionospheric F2 critical frequency at low latitude. *Journal of Atmospheric and Solar-Terrestrial Physics*, *100*, 24–33. https://doi.org/10.1016/j.jastp.2013.03.012

Johnson, F. S. (1964). Composition changes in the upper atmosphere. In E. Thrane (Ed.), *Electron density distributions in the ionosphere and exosphere* (pp. 81–84). North Holland.

Jones, W. B., Graham, R. P., & Leftin, M. (1969). *Advances in ionospheric mapping by numerical methods. ESSA Technical Report ERL 107-ITS75*. U.S. Department of Commerce.

Lean, J. L., Warren, H. P., Mariska, J. T., & Bishop, J. (2003). A new model of solar EUV irradiance variability: 2. Comparisons with empirical models and observations and implications for space weather. *Journal of Geophysical Research*, *108*(A2), 1059. https://doi.org/10.1029/2001JA009238

Liemohn, M. W., Shane, A. D., Azari, A. R., Petersen, A. K., Swiger, B. M., & Mukhopadhyay, A. (2021). RMSE is not enough: Guidelines to robust data-model comparisons for magnetospheric physics. *Journal of Atmospheric and Solar-Terrestrial Physics*, *218*, 105624. https://doi.org/10.1016/j.jastp.2021.105624

LISIRD. (2005). FISM2 daily averages [Dataset]. Laboratory for Atmospheric Physics (LASP) Interactive Solar Irradiance Datacenter (LISIRD). Retrieved from https://lasp.colorado.edu/lisird/data/fism_daily_hr

Liu, H., Shah, S., & Jiang, W. (2004). On-line outlier detection and data cleaning. *Computers & Chemical Engineering*, *28*(9), 1635–1647. https://doi.org/10.1016/j.compchemeng.2004.01.0

Liu, L., He, M., Yue, X., Ning, B., & Wan, W. (2010). Ionosphere around equinoxes during low solar activity. *Journal of Geophysical Research*, *115*(A9), A09307. https://doi.org/10.1029/2010JA015318

Liu, L., Wan, W., Ning, B., Pirog, O. M., & Kurkin, V. I. (2006). Solar activity variations of the ionospheric peak electron density. *Journal of Geophysical Research*, *111*(A8), A08304. https://doi.org/10.1029/2006JA011598

Lühr, H., & Xiong, C. (2010). IRI-2007 model overestimates electron density during the 23/24 solar minimum. *Geophysical Research Letters*, *37*(23), L23101. https://doi.org/10.1029/2010GL045430

Ma, R., Xu, J., Wang, W., & Yuan, W. (2009). Seasonal and latitudinal differences of the saturation effect between ionospheric NmF2 and solar activity indices. *Journal of Geophysical Research*, *114*(A10), A10303. https://doi.org/10.1029/2009JA014353

Mayr, H. G., & Mahajan, K. K. (1971). Seasonal variation in the F2 region. *Journal of Geophysical Research*, *76*(4), 1017–1027. https://doi.org/10.1029/JA076i004p01017

McClintock, W. E., Rottman, G. J., & Woods, T. N. (2005). Solar-stellar irradiance comparison experiment II (Solstice II): Instrument concept and design. *Solar Physics*, *230*(1–2), 225–258. https://doi.org/10.1007/s11207-005-7432-x

Millward, G. H., Rishbeth, H., Fuller-Rowell, T. J., Aylward, A. D., Quegan, S., & Moffett, R. J. (1996). Ionospheric F 2 layer seasonal and semiannual variations. *Journal of Geophysical Research*, *101*(A3), 5149–5156. https://doi.org/10.1029/95JA03343

Moffett, R. J. (1979). Equatorial anomaly in the electron distribution of the terrestrial F-region. *Fundamentals of Cosmic Physics*, *4*. [Quiet-time behavior, variations].

Murphy, A. H. (1988). Skill scores based on the mean square error and their relationships to the correlation coefficient. *Monthly Weather Review*, *116*(12), 2417–2424. https://doi.org/10.1175/1520-0493(1988)116%3C2417:SSBOTM%3E2.0.CO;2

Nava, B., Coisson, P., & Radicella, S. M. (2008). A new version of the NeQuick ionosphere electron density model. *Journal of Atmospheric and Solar-Terrestrial Physics*, *70*(15), 1856–1862. https://doi.org/10.1016/j.jastp.2008.01.015

Perna, L., Pezzopane, M., Ezquer, R., Cabrera, M., & Baskaradas, J. A. (2017). NmF2 trends at low and mid latitudes for the recent solar minima and comparison with IRI-2012 model. *Advances in Space Research*, *60*(2), 363–374. https://doi.org/10.1016/j.asr.2016.09.025

Raghavarao, R., Nageswararao, M., Sastri, J. H., Vyas, G. D., & Sriramarao, M. (1988). Role of equatorial ionization anomaly in the initiation of equatorial spread-F. *Journal of Geophysical Research*, *93*(A6), 5959–5964. https://doi.org/10.1029/JA093iA06p05959

Rajaram, G. (1977). Structure of the equatorial F region, topside and bottomside: A review. *Journal of Atmospheric and Terrestrial Physics*, *39*(9–10), 1125–1144. https://doi.org/10.1016/0021-9169(77)90021-6

Reinisch, B. W., & Galkin, I. A. (2011). Global ionospheric radio observatory (GIRO). *Earth Planets and Space*, *63*(4), 377–381. https://doi.org/10.5047/eps.2011.03.001

Richards, P. G., Fennelly, J. A., & Torr, D. G. (1994). EUVAC: A solar EUV flux model for aeronomic calculations. *Journal of Geophysical Research*, *99*(A5), 8981–8992. https://doi.org/10.1029/94JA00518

Richards, P. G., Woods, T. N., & Peterson, W. K. (2006). HEUVAC: A new high resolution solar EUV proxy model. *Advances in Space Research*, *37*(2), 315–322. https://doi.org/10.1016/j.asr.2005.06.031

Rishbeth, H., & Muller-Wodarg, I. C. F. (2006). Why is there more ionosphere in January than in July? The annual asymmetry in the F2-layer. *Annales de Geophysique*, *24*(12), 3293–3311. https://doi.org/10.5194/angeo-24-3293-2006

Rishbeth, H., & Setty, C. S. G. K. (1961). The F-layer at sunrise. *Journal of Atmospheric and Solar-Terrestrial Physics*, *21*(4), 263–276. https://doi.org/10.1016/0021-9169(61)90205-7

Rush, M. C., PoKempner, M., Anderson, D. N., Perry, J., Steward, F. G., & Reasoner, R. (1984). Maps of foF2 derived from observations and theoretical data. *Radio Science*, *19*(4), 1083–1097. https://doi.org/10.1029/RS019i004p01083

Sai Gowtam, V., & Tulasi Ram, S. (2017). Ionospheric winter anomaly and annual anomaly observed from Formosat-3/COSMIC Radio Occultation observations during the ascending phase of solar cycle 24. *Advances in Space Research*, *60*(8), 1585–1593. https://doi.org/10.1016/j.asr.2017.03.017

Schonfeld, S. J., White, S. M., Henney, C. J., Hock-Mysliwiec, R. A., & McAteer, R. T. J. (2019). The slowly varying Corona. II. The components of F10. 7 and their use in EUV proxies. *The Astrophysical Journal*, *884*(2), 141. https://doi.org/10.3847/1538-4357/ab3af9

Singh, D., & Goncharenko, L. (2024). Regional NmF2 empirical models (version v3) [Software]. *Zenodo*. https://doi.org/10.5281/zenodo.13256130

Snow, M., McClintock, W. E., Woods, T. N., White, O. R., Harder, J. W., & Rottman, G. (2005). The Mg II index from SORCE. *Solar Physics*, *230*(1–2), 325–344. https://doi.org/10.1007/s11207-005-6879-0

Tapping, K., & Morgan, C. (2017). Changing relationships between sunspot number, total sunspot area and F 10.7 in Cycles 23 and 24. *Solar Physics*, *292*(6), 73. https://doi.org/10.1007/s11207-017-1111-6

Tapping, K. F. (2013). The 10.7 cm solar radio flux (F10.7). *Space Weather*, *11*(7), 394–406. https://doi.org/10.1002/swe.20064

Tapping, K. F., & Charrois, D. P. (1994). Limits to the accuracy of the 10.7 cm flux. *Solar Physics*, *150*(1–2), 305–315. https://doi.org/10.1007/BF00712892

Thiemann, E. M., Eparvier, F. G., Woodraska, D., Chamberlin, P. C., Machol, J., Eden, T., et al. (2019). The GOES-R EUVS model for EUV irradiance variability. *Journal of Space Weather and Space Climate*, *9*, A43. https://doi.org/10.1051/swsc/2019041

Tobiska, W. K. (2004). SOLAR2000 irradiances for climate change research, aeronomy, and space system engineering. *Advances in Space Research*, *34*(8), 1736–1746. https://doi.org/10.1016/j.asr.2003.06.032

Torr, M. R., & Torr, D. G. (1973). The seasonal behavior of the F2-layer of the ionosphere. *Journal of Atmospheric and Solar-Terrestrial Physics*, *35*(12), 2237–2251. https://doi.org/10.1016/0021-9169(73)90140-2

Vautard, R., & Ghil, M. (1989). Singular spectrum analysis in nonlinear dynamics, with applications to paleoclimatic time series. *Physica D: Nonlinear Phenomena*, *35*(3), 395–424. https://doi.org/10.1016/0167-2789(89)90077-8

Vautard, R., Yiou, P., & Ghil, M. (1992). Singular-spectrum analysis: A toolkit for short, noisy chaotic signals. *Physica D: Nonlinear Phenomena*, *58*(1–4), 95–126. https://doi.org/10.1016/0167-2789(92)90103-T

Volland, H. (1969). The upper atmosphere as a multiple refractive medium for neutral air motions. *Journal of Atmospheric and Solar-Terrestrial Physics*, *31*(4), 491–514. https://doi.org/10.1016/0021-9169(69)90002-6

Walker, G. O. (1981). Longitudinal structure of the equatorial ionization anomaly: A review. *Journal of Atmospheric and Terrestrial Physics*, *43*, 763–775. https://doi.org/10.1016/0021-9169(81)90052-0

Warren, H. P., Mariska, J. T., & Lean, J. (2001). A new model of solar EUV irradiance variability: 1. Model formulation. *Journal of Geophysical Research*, *106*(A8), 15745–15757. https://doi.org/10.1029/2000JA000282

WDC for Ionosphere and Space Weather. (n.d.). Manually scaled ionosonde data [Dataset]. World Data Center (WDC) for Ionosphere and Space Weather at National Institute of Information and Communication Technology, Tokyo. Retrieved from https://wdc.nict.go.jp/Ionosphere/en/archive/isdj_manual_txt.html

Woods, T. N., Eparvier, F. G., Bailey, S. M., Chamberlin, P. C., Lean, J., Rottman, G. J., et al. (2005). Solar EUV Experiment (SEE): Mission overview and first results. *Journal of Geophysical Research*, *110*(A1), A01312. https://doi.org/10.1029/2004JA010765

Woods, T. N., Eparvier, F. G., Harder, J., & Snow, M. (2018). Decoupling solar variability and instrument trends using the multiple same-irradiance-level (MuSIL) analysis technique. *Solar Physics*, *293*(5), 1–21. https://doi.org/10.1007/s11207-018-1294-5

Woods, T. N., Eparvier, F. G., Hock, R., Jones, A. R., Woodraska, D., Judge, D., et al. (2012). Extreme ultraviolet variability experiment (EVE) on the solar dynamics observatory (SDO): Overview of science objectives, instrument design, data products, and model developments. *Solar Physics*, *275*(1–2), 115–143. https://doi.org/10.1007/s11207-009-9487-6

Woods, T. N., Tobiska, W. K., Rottman, G. J., & Worden, J. R. (2000). Improved solar Lyman α irradiance modeling from 1947 through 1999 based on UARS observations. *Journal of Geophysical Research*, *105*(A12), 27195–27216. https://doi.org/10.1029/2000JA000051

Yamazaki, Y., Matzka, J., Stolle, C., Kervalishvili, G., Rauberg, J., Bronkalla, O., et al. (2022). Geomagnetic activity index Hpo. *Geophysical Research Letters*, *49*(10), e2022GL098860. https://doi.org/10.1029/2022GL098860

Yonezawa, T. (1971). The solar-activity and latitudinal characteristics of the seasonal, non-seasonal and semi-annual variations in the peak electron densities of the F2-layer at noon and at midnight in middle and low latitudes. *Journal of Atmospheric and Terrestrial Physics*, *33*(6), 889–907. https://doi.org/10.1016/0021-9169(71)90089-4

Zossi, B. S., Duran, T., Medina, F. D., de Haro Barbas, B. F., Melendi, Y., & Elias, A. G. (2023). Evaluating F2-region long-term trends using the International Reference Ionosphere (IRI) model: Is this a feasible approximation for experimental trends? *Atmospheric Chemistry and Physics*, *23*(21), 13973–13986. https://doi.org/10.5194/acp-23-13973-2023